


Article

Investigation on the Catalytic Cracking Mechanism of CuO on Dimethyl Sulfoxide (C₂H₆OS) and Surface Modification Effects: Insights from Density Functional Theory Calculations

Yan-Qun Wang ^{1,2,3} , Xiang-Long Meng ^{1,2}, Hao-Hai Xia ³, Jian-Zheng Su ¹, Li-Lin Lu ⁴  and Wei-Chu Yu ^{3,*}

¹ State Key Laboratory of Shale Oil and Gas Enrichment Mechanisms and Effective Development, Beijing 100083, China; qunqunlucky@whu.edu.cn (Y.-Q.W.)

² State Center for Research and Development of Oil Shale Exploitation, Beijing 100083, China

³ College of Chemistry and Environmental Engineering, Yangtze University, Jingzhou 434023, China

⁴ State Key Laboratory of Refractories and Metallurgy, Wuhan University of Science and Technology, Wuhan 430081, China

* Correspondence: yuweichu@126.com; Tel.: +86-716-8060-650

Abstract: To explore the catalytic cracking mechanism of CuO on oil shale and the catalytic activity of surface modifications of CuO on oil shale, dimethyl sulfoxide (C₂H₆OS) is used as a model molecule representative of organic sulfur compounds in oil shale, and the adsorption and dissociation behaviors of C₂H₆OS molecules on pure and OH pre-adsorbed CuO(111) surfaces were investigated by density functional theory calculations. The results indicate that C₂H₆OS selectively adsorbs at the Cu_{sub} sites via the S atom and decomposes through cleavage of the C–H bond prior to the breaking of the C–S bond on both surfaces. The presence of OH on the CuO(111) surface promoted the dissociation of C₂H₆OS. The energy barriers of dehydrogenation and desulfurization of C₂H₆OS on the OH pre-adsorbed CuO(111) surface were 20.0 and 19.3 kcal/mol, respectively, which are 41% and 49% lower than those on pure surfaces. The present results provide crucial guidance for the synthesis and improvement of high-performance pyrolysis catalysts specifically designed for oil shale applications. Additionally, they also present important data regarding to the thermal stability of C₂H₆OS in the presence of incompatible substances.

Keywords: oil shale; pyrolysis; catalytic activity; dimethyl sulfoxide; nano copper oxide; decomposition mechanism



Citation: Wang, Y.-Q.; Meng, X.-L.; Xia, H.-H.; Su, J.-Z.; Lu, L.-L.; Yu, W.-C. Investigation on the Catalytic Cracking Mechanism of CuO on Dimethyl Sulfoxide (C₂H₆OS) and Surface Modification Effects: Insights from Density Functional Theory Calculations. *Processes* **2023**, *11*, 1781. <https://doi.org/10.3390/pr11061781>

Academic Editor: Zahra Gholami

Received: 27 April 2023

Revised: 2 June 2023

Accepted: 6 June 2023

Published: 11 June 2023



Copyright: © 2023 by the authors. Licensee MDPI, Basel, Switzerland. This article is an open access article distributed under the terms and conditions of the Creative Commons Attribution (CC BY) license (<https://creativecommons.org/licenses/by/4.0/>).

1. Introduction

Oil shale is a solid underground resource with low maturity; it is difficult to exploit compared with traditional energy sources such as oil and coal [1]. Pyrolysis is a popular method of converting oil shale into high-quality liquid fuel. The addition of appropriate catalysts can significantly enhance the thermal conversion efficiency of kerogen in oil shale, thereby improving the quality of the oil and gas products.

Recently, metal-based catalysts, especially metal oxides, have attracted significant attention owing to their excellent catalytic performances. They are believed to lead to high desulfurization rates of shale oil or low-sulfur diesel [2,3]. Chen et al. [4] demonstrated the effectiveness of CuO nanoparticles as hydrothermal cracking catalysts in reducing the viscosity of heavy oil from the Shengli Oilfield by 94.6% and transforming 22.4% of asphaltene into lighter components. Zhong et al. [5] further investigated the use of CuO nanoparticles in the catalytic pyrolysis of heavy oil and observed that the addition of a THF donor in the catalytic reaction further reduced the viscosity. Furthermore, a recent density functional theory (DFT) study [6] reported the catalytic activity of several transition metal ions in the hydrothermal degradation of heavy oil; they found the order of catalytic activity as Cu²⁺ > Co²⁺ ≈ Ni²⁺ > Fe²⁺, with Cu²⁺ exhibiting the highest catalytic activity.

In our recent theoretical study on the catalytic activity of Cu-doped SBA-15 molecular sieves, we found that the decomposition of organic sulfur compounds can be promoted by doping with Cu [7]. Moreover, research [8] has shown that Fe, Ca, Zn, Ni, and other metal oxides and chloride expedite the pyrolysis of oil shale, facilitate the generation of hydrogen-free radicals, and cause the shale oil to become lighter. Lu et al. [9] used MgO as a catalyst to investigate the catalytic pyrolysis of Changji oil shale in Xinjiang and found that the addition of MgO increased the yields of olefins and shale gas CH₄ in shale oil. Wang et al. [8] reported that Fe₂O₃ has a better catalytic effect on oil shale pyrolysis as it increases the yield of shale oil. Esen et al. [10] studied the catalytic pyrolysis of Turkish oil shale and found that the liquefaction rate was 23.4% at a concentration of 3% MoO₃, and that the catalytic effect of MoO₃ was better than that of Fe₂O₃. Given the effectiveness of metal oxides in oil shale cracking and the favorable catalytic properties of Cu-based catalysts in heavy oil cracking, CuO could possibly serve as an effective catalyst for oil shale cracking. Nevertheless, research on the specific catalytic effect of CuO on oil shale cracking is limited and the interaction mechanism between CuO and oil shale remains unclear.

The pyrolysis of kerogen in oil shale is highly complex because of its macromolecular organic structure. Therefore, elucidating the catalytic pyrolysis mechanism for oil shale is challenging. The application of molecular simulation technology can offer insights into the intricate changes that occur during catalytic transformation of complex molecular systems and provide a novel understanding of the underlying reaction mechanism. Guo et al. [11] utilized DFT and found that the decomposition process of H₂O₂ on CuO and Ag-doped CuO surfaces follows the sequence of H₂O₂ → 2OH → H₂O + O, with the decomposition of H₂O₂ being comparatively easier on the Ag-doped CuO surface than on the pure CuO surface. Ahmad et al. [12] employed dispersive-corrected Hubbard DFT to demonstrate that the decomposition of H₂O into OH and H occurs on the surface of CuO(111), with the oxygen-preadsorbed surface exhibiting the lowest reaction energy. Ye et al. [13] employed ab initio quantum chemistry to elucidate the mechanism of the thermochemical reactions between organic carbon and H radicals during oil shale retorting. Tian et al. [14] investigated the impact of electric fields on the macromolecular structure of kerogen at the M06-2X/6-311+G(d,p) level using DFT and established different reaction pathways. Chen et al. [15] employed quantum chemical simulations and kinetic analysis to investigate the formation mechanism of nitrogen-containing substances during the pyrolysis of oil shale and obtained the energies of reactants, transition states, and intermediates involved in the reaction. Despite these studies, limited research has been conducted on the catalytic cracking mechanism of oil shale at the molecular level.

Kang et al. [16] reported that the rupture of heteroatomic bonds is crucial for increasing the cracking rate of kerogen. They found that FeCl₃ promotes the rupture of heteroatomic bonds in kerogen and ring-opening reaction of aromatic structures, and that the rupture of heteroatomic bonds triggers a chain reaction network for the cracking of kerogen. To understand the catalytic pyrolysis mechanism of macromolecular aggregates, such as kerogen, the breaking of heteroatomic bonds in kerogen induced by catalysts must be investigated. The principal heteroatoms in kerogen are N and S, with the S atoms existing primarily as sulfone and sulfoxide. Dimethyl sulfoxide (C₂H₆OS) is a commonly used sulfoxide. In a recent study [7], we selected C₂H₆OS as a model molecule for organic sulfur in oil shale and investigated its interaction with SBA-15 molecular sieves. To further investigate the interaction mechanisms between organic sulfur compounds in oil shale and different types of catalysts, the present study also employed C₂H₆OS as the model molecule. The interactions of C₂H₆OS with nano-CuO were examined using the DFT to determine the adsorption configuration, adsorption energy, and pyrolysis activation energy; additionally, the mechanism of the catalytic pyrolysis of C₂H₆OS by nano-CuO and activities of surface modifications of nano-CuO were studied. These theoretical findings are expected to provide valuable guidance for the design and development of catalysts for oil shale pyrolysis under specific conditions. Moreover, further comprehensive investigations are necessary to explore the thermal stability of C₂H₆OS, considering the potential risk

of explosions associated with its thermal decomposition. Thus, the results of this study also contribute valuable evaluation data regarding the thermal stability of C₂H₆OS in the presence of incompatible substances.

2. Computational Method

The DMol³ software package [17] was utilized for all DFT calculations, with the electron exchange and correlation energy calculated using the Perdew–Wang (PW91) functional [18] based on the generalized gradient approximation (GGA) [19]. All electron double numerical (DND) [20] basis sets that include a d-type polarized function on all non-hydrogen atoms were utilized. Numerical basis sets are well-known for their ability to minimize or eliminate basis set superposition errors (BSSE) [21] and are thus highly valuable for the investigation of chemical reactions. Given that the CuO bulk possesses an antiferromagnetic ground state, the spin was not restricted in the calculations [22,23]. According to the literature [24], the DFT semi-core pseudopot (DSPP) [25] was utilized for the treatment of Cu atoms so that the electron behavior of Cu atoms can be described more accurately. Additionally, to ensure precise depiction of the van der Waals (VDW) interactions, the DFT-D₃ method developed by Grimme et al. [26] was employed for correction of dispersion forces. The Broyden–Fletcher–Goldfarb–Shanno (BFGS) method [27] was employed for structure relaxation. The transition states of each reaction were studied using the linear/quadratic synchronous transit (LST/QST) method [28] and were verified through frequency analysis. The Brillouin region was integrated using a 3 × 3 × 1 k point grid sampled by the Monkhorst–Pack scheme. The cut-off value for real space was set to 4.2 Å. The convergence standard of optimization was that the total energy change of two adjacent steps in the optimization process was less than 2 × 10^{−5} eV, the energy gradient was less than 0.004 eV/Å, and the atomic coordinate change was less than 0.005 Å.

Slab periodic models are commonly used to investigate surface reactions on catalysts or materials. A slab periodic model of a CuO(111) surface was adopted in view of its thermodynamically stability [29] in this work. A 4 × 2 supercell was used on the side plane with a thickness of 9 layers. The model comprises a total of 64 atoms (Cu₃₂O₃₂), with a vacuum layer thickness of 15 Å. All atoms were relaxed in all of the geometry optimization calculations.

To determine the adsorption energy, the formula $E_{ads} = E_{mol} + E_{slab} - E_{(mol+slab)}$ was employed, where E_{mol} denotes the energy of the C₂H₆OS molecule in a cubic cell with dimensions of 15 Å × 15 Å × 15 Å, E_{slab} represents the minimum energy of the CuO(111) surface, and $E_{(mol+slab)}$ corresponds to the total energy of the CuO(111) surface in conjunction with the C₂H₆OS molecule. Based on this definition, the positive adsorption energy is associated with a stable adsorption phenomenon [30].

3. Results and Discussion

Two reaction environments were constructed in this work to account for the possible surface groups present on the CuO surface when preparing nano-CuO using Cu(OH)₂, as reported in the literature [4], and the complex conditions encountered when CuO is used for underground in situ catalysis, specifically, the pure CuO(111) (a) and OH pre-adsorbed CuO(111) (b) surfaces, as shown in Figure 1 which displays the optimized structures for both surfaces. The pure CuO(111) surface contains four unique adsorption sites known as “Cu_{suf}”, “Cu_{sub}”, “O_{suf}”, and “O_{sub}”. Among these, “Cu_{suf}” and “O_{suf}” are located in the outermost layer, whereas “Cu_{sub}” and “O_{sub}” are situated in the subouter layer. Moreover, the outermost layer’s Cu_{sub} atoms are tetra-coordinated, while the subouter layer’s Cu_{sub} atoms are tri-coordinated. The outermost layer’s O_{suf} atoms are tri-coordinated, and the subouter layer’s O_{sub} atoms are tetra-coordinated.

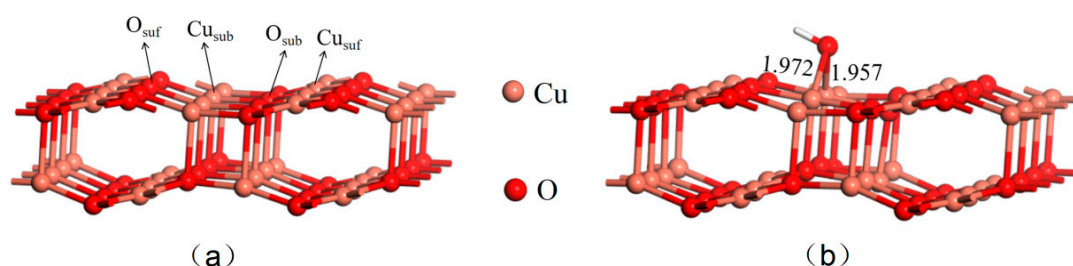


Figure 1. Structures of the (a) pure CuO(111) surface and (b) OH pre-adsorbed CuO(111) surface.

3.1. Adsorption Structures and Energies of C_2H_6OS on the Pure CuO(111) Surface

The C_2H_6OS molecule exhibited a strong affinity toward the Lewis acid site, i.e., the Cu ion on the CuO surface, wherein the O and S atoms in the molecule were responsible for anchoring the adsorbate onto the surface. Four types of adsorption on a pure CuO(111) surface are known, wherein the S and O atoms of the molecule are in proximity to the Cu_{suf} and Cu_{sub} atoms, as shown in Figure 2. For ease of discussion, the notation “DS” is employed to denote the stable configuration for C_2H_6OS adsorbed on the pure CuO(111) surface.

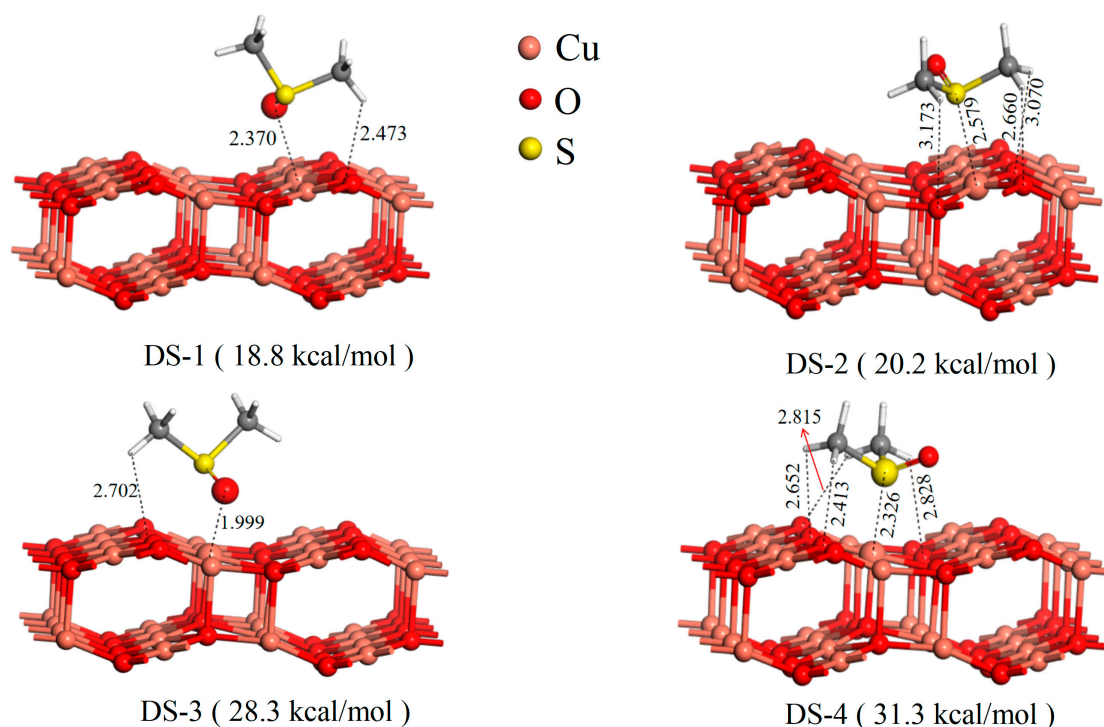


Figure 2. Optimized structures and adsorption energies of C_2H_6OS on the pure CuO(111) surface.

In Figure 2, DS-1 and DS-2 correspond to the stable structures of the O and S atoms adsorbed on Cu_{suf} , whereas DS-3 and DS-4 depict the stable structures of the O and S atoms adsorbed on Cu_{sub} , respectively. Notably, the adsorption energies presented in Figure 2 suggest that the interaction of the S atom in C_2H_6OS molecule with the Cu atom on the surface is stronger than that of the O atom with the surface Cu atom. Moreover, the Cu atom in the subouter layer exhibited stronger adsorption affinity compared with the outermost Cu atom, thus suggesting that the subouter-layer Cu atom plays a crucial role in the adsorption process. The interaction between the S atom in the molecule and Cu atom on the subouter layer of the surface formed the most stable adsorption structure (DS-4). The bond length between S and Cu in DS-4 was 2.326 Å, and the corresponding adsorption energy was 31.3 kcal/mol, thus indicating a chemical adsorption behavior. The second most stable structure (DS-3) involved the adsorption of an O atom onto a Cu_{sub} atom, with an O–Cu bond length of 1.999 Å and adsorption energy of 28.3 kcal/mol. The

adsorption structures formed by the S and O atoms with the Cu_{suf} atoms (i.e., DS-1 and DS-2) had longer S–Cu and O–Cu bond lengths (2.579 and 2.370 Å, respectively) than those formed by the Cu_{sub} atoms, thus indicating weaker interactions. The adsorption energies for DS-1 and DS-2 were 20.2 and 18.8 kcal/mol, respectively, which are lower than those for the structures formed with the subouter Cu atoms.

3.2. Adsorption Structures and Energies of $\text{C}_2\text{H}_6\text{OS}$ on the OH Pre-Adsorbed $\text{CuO}(111)$ Surface

The adsorption of $\text{C}_2\text{H}_6\text{OS}$ on the OH pre-adsorbed $\text{CuO}(111)$ surface occurred on the Lewis acid sites via the O and S atoms in the molecule. This study focused primarily on the $\text{C}_2\text{H}_6\text{OS}$ molecules in the vicinity of OH, essentially resulting in four types of adsorption. These include the adsorption of the S and O atoms in the molecule close to the Cu_{suf} atoms, and those close to the Cu_{sub} atoms near the OH on the surface, as depicted in Figure 3. To facilitate the description, “DS-OH” is used to represent the stable adsorption structure of $\text{C}_2\text{H}_6\text{OS}$ on the OH preadsorbed $\text{CuO}(111)$ surface.

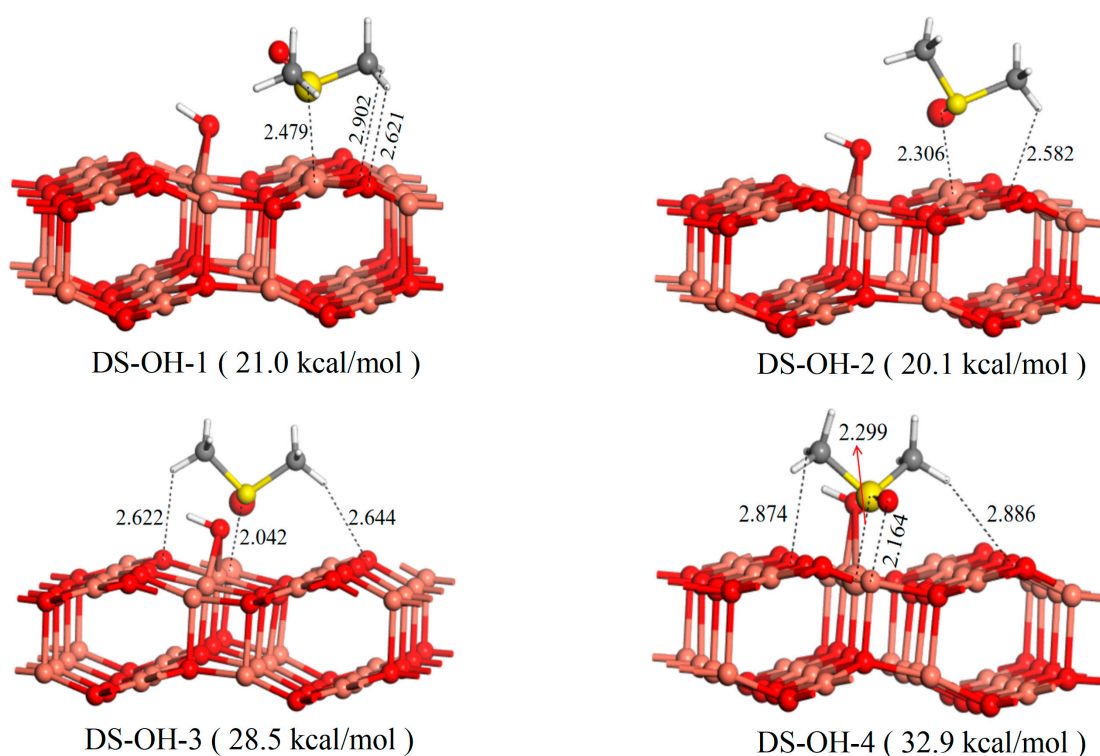


Figure 3. Optimized structures and adsorption energies of $\text{C}_2\text{H}_6\text{OS}$ on the OH preadsorbed $\text{CuO}(111)$ surface.

In Figure 3, DS-OH-1 and DS-OH-2 represent the stable adsorption configurations of S and O atoms in the $\text{C}_2\text{H}_6\text{OS}$ molecules adsorbed with Cu_{suf} atoms, whereas DS-OH-3 and DS-OH-4 correspond to the stable adsorption configurations of O and S atoms adsorbed with Cu_{sub} atoms near OH. As illustrated in Figure 3, little difference was noted in the adsorption energies for $\text{C}_2\text{H}_6\text{OS}$ on the OH preadsorbed $\text{CuO}(111)$ surface compared with the pure $\text{CuO}(111)$ surface regardless of the type of adsorption, thus indicating that the preadsorption of OH does not significantly affect the adsorption of $\text{C}_2\text{H}_6\text{OS}$ molecules on the $\text{CuO}(111)$ surface. The most stable adsorption structure (DS-OH-4) was characterized by the adsorption of S atoms in the molecule and Cu_{sub} atoms near the surface OH. Notably, the S–Cu bond length in DS-OH-4 was 2.299 Å, which is shorter than that on the pure surface (2.326 Å). Moreover, the corresponding adsorption energy for DS-OH-4 was 32.9 kcal/mol, which is higher than that on the pure surface. The second most stable structure (DS-OH-3) corresponds to the adsorption of the O atom in the molecule and the Cu_{sub} atom near the surface OH. In particular, the O–Cu bond length in DS-OH-3 was 2.042 Å, and the

corresponding adsorption energy was 28.5 kcal/mol, which is almost equal to that of the pure surface.

To further understand the interaction between C_2H_6OS and the pure or OH pre-adsorbed $CuO(111)$ surface, the electronic structures of the most stable adsorption configurations, DS-4 and DS-OH-4, were analyzed. The partial densities of states (PDOS) of these configurations before and after C_2H_6OS adsorption are shown in Figure 4. Evidently, both the s-PDOS and p-PDOS of S in C_2H_6OS exhibited a leftward shift, with the p-PDOS of S moving to a lower energy compared with the initial configuration. Moreover, after adsorption, the S p-PDOS interacted with the Cu p-PDOS at -2.09 and -4.99 eV on the pure $CuO(111)$ surface, thus implying the presence of strong interactions between C_2H_6OS and the pure $CuO(111)$ surface. In the case of OH preadsorbed $CuO(111)$ surface, the S p-PDOS interacted with the Cu p-PDOS by state overlap at -3.16 and -5.03 eV, as shown in Figure 4b. These energies correspond to the S–Cu bonds in DS-OH-4. The characteristic peaks of the p orbitals near the Fermi level became wider after adsorption, thus indicating a significant delocalization of the p orbitals of the S atom in C_2H_6OS .

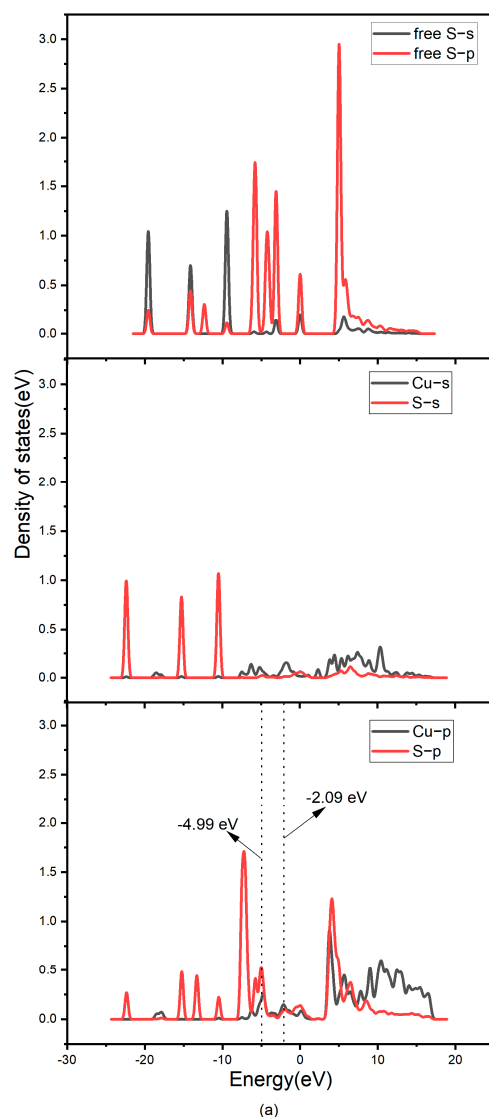


Figure 4. Cont.

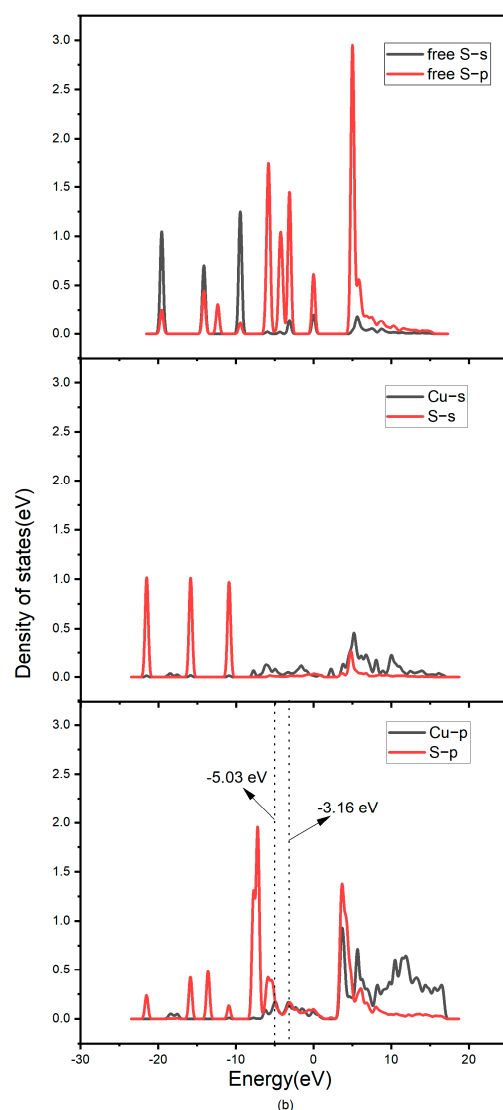


Figure 4. PDOS of the most stable configurations for C_2H_6OS on the $CuO(111)$ surface before and after adsorption. Configuration on (a) pure $CuO(111)$ surface and (b) OH preadsorbed $CuO(111)$ surface.

3.3. Decomposition of C_2H_6OS on the Pure and OH Pre-Adsorbed $CuO(111)$ Surfaces

3.3.1. Decomposition of C_2H_6OS on the Pure $CuO(111)$ Surface

As illustrated in Figure 2, DS-4 was the most stable configuration. Accordingly, DS-4 served as the initial state for subsequent analyses. C_2H_6OS contains three types of bonds, namely C–H, C–S, and S=O. Because double bonds possess a higher bond energy compared with single bonds, this study focused primarily on the breaking of C–H and C–S bonds. First, from the DS-4 configuration, numerous possible C–H and C–S bond breaks were explored to identify transition states. Subsequently, the activation energies associated with each reaction pathway were compared to determine the preferentially broken bonds, and three main reaction pathways were identified. Table 1 lists the intermediate relative energies, reaction energy barriers, and reaction heats of the three main reaction pathways. The structures of the intermediates, transition states, and products of each pathways are shown in Figure S1.

Table 1. Intermediate relative energy E_{ad} (kcal/mol), reaction energy barrier E_b (kcal/mol), and reaction heat E_r (kcal/mol) for the dissociation of C–H and C–S bonds of C_2H_6OS on the pure $CuO(111)$ surface.

Reaction Path	Bond That Is Broken	E_{ad}	E_b	E_r
$H \rightarrow O_{suf}$	C–H	−31.3	33.9	6.4
$-CH_3 \rightarrow O_{suf}$	C–S	−31.3	58.2	−3.2
$-CH_3 \rightarrow Cu_{sub}$	C–S	−31.3	59.8	13.9
$-CH_2 \rightarrow O_{suf}$	C–S	−24.9	38.1	−9.6
$-CH_2 \rightarrow Cu_{sub}$	C–S	−24.9	50.0	31.5

Evidently from Table 1, on the pure $CuO(111)$ surface, the transfer of an H atom from C_2H_6OS to the O_{suf} site had a lower energy barrier (33.9 kcal/mol) compared with the C–H bond energies (96–99 kcal/mol) reported in the literature [31,32]. Note that, if a $-CH_3$ group of C_2H_6OS transfers to the O_{suf} and Cu_{sub} sites, the energy barriers were 58.2 and 59.8 kcal/mol, respectively. Therefore, when C_2H_6OS molecules were adsorbed onto the pure $CuO(111)$ surface, the H atom in C_2H_6OS was preferentially transferred to the O_{suf} site to generate C_2H_5OS and H. The C–H bond rupture occurred via a seven-center transition state (TS1). The S and C atoms in the intermediate C_2H_5OS (see IM2 in Figure 5) formed stable chemical bonds with the surface Cu atoms, with bond lengths of 2.261 and 2.003 Å, respectively, and the H atoms formed a hydroxyl group with the surface O atoms. The intermediate state, transition state, and product structures of the process are shown in Figure 5; the energy path of the reaction is shown in Figure 6.

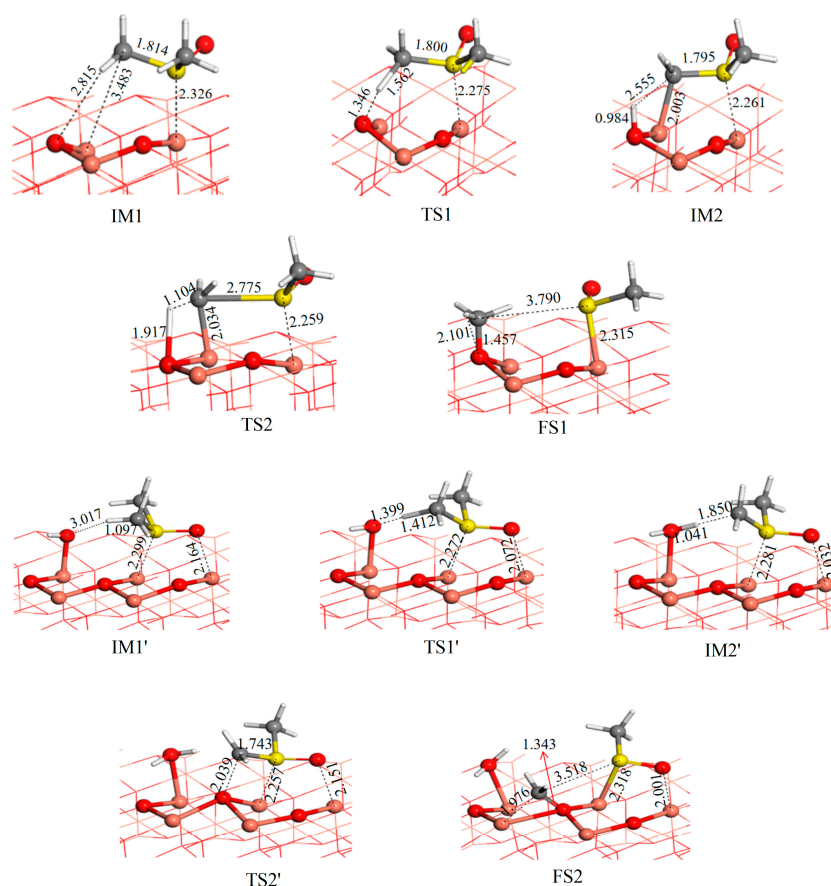


Figure 5. Structure of intermediates (IM), transition states (TS), and final state (FS) on the lowest energy path for dehydrogenation and C–S bond cleavage of C_2H_6OS on the pure and OH pre-adsorbed $CuO(111)$ surfaces.

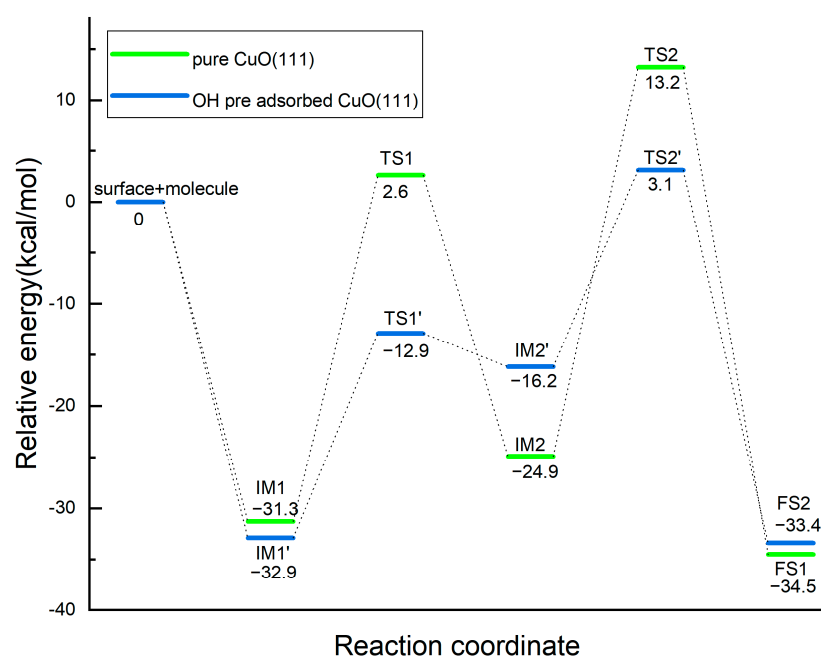


Figure 6. Lowest energy pathways of dehydrogenation and C–S bond cleavage of C_2H_6OS on the pure and OH preadsorbed $CuO(111)$ surfaces.

The intermediate C_2H_5OS (IM2 in Figure 5) underwent further C–H and C–S bond cleavage on the pure $CuO(111)$ surface. Various possibilities for C–H and C–S bond cleavage were considered; however, no stable configuration with C–H bond cleavage was identified. Instead, two dissociative structures resulting from the C–S bond cleavage were observed. These structures involve the $-CH_2$ group attacking either the O_{suf} of the surface OH or the Cu_{sub} atom near the OH, and thereby resulting in C–S bond cleavage (Figure S2). The Gibbs free energy changes at room temperature for these two processes were calculated and are listed in Table 2. The results reveal that the transfer of $-CH_2$ to the O_{suf} site represents a thermodynamically stable reaction with a -11.4 kcal/mol change in Gibbs free energy. By contrast, if $-CH_2$ is transferred to the Cu_{sub} site, then 26.4 kcal/mol energy must be overcome for the reaction to occur. Furthermore, the energy barriers for both processes were calculated and revealed that if $-CH_2$ is transferred to the O_{suf} site, then 38.1 kcal/mol through the transition state TS2 must be overcome, as shown in Figure 6; this value is much lower than that reported (66 kcal/mol) [31,32] for a typical C–S bond breakage. Finally, if $-CH_2$ is instead transferred to the Cu_{sub} site, then 50.0 kcal/mol must be overcome, indicating that the transfer of $-CH_2$ from the IM2 intermediate state toward the O_{suf} site represents both a thermodynamically and kinetically favorable reaction path.

Table 2. Gibbs free energy change (kcal/mol) of C–H and C–S bond dissociation reactions of intermediate IM2 and IM2' on the $CuO(111)$ surface.

		$CH_2 \rightarrow O_{suf}$	$CH_2 \rightarrow Cu_{sub}$	$CH_2 \rightarrow O_{suf}$	$H \rightarrow O_{sub}$	$H \rightarrow O_{suf}$
ΔG	Pure $CuO(111)$	-11.4	26.4			
	OH pre-adsorbed $CuO(111)$			-17.0	10.3	16.7

3.3.2. Decomposition Reaction of C_2H_6OS on the OH Pre-Adsorbed $CuO(111)$ Surface

The most stable adsorption configuration of C_2H_6OS on the OH pre-adsorbed $CuO(111)$ surface, denoted as DS-OH-4 in Figure 3, served as the initial state for exploring the breaking of various C–H and C–S bonds in the molecule on the OH pre-adsorbed $CuO(111)$ surface. Thus, five main reaction pathways were determined. The intermediate relative energies, reaction energy barriers, and reaction heats for each pathway are listed in Table 3.

The intermediates, transition states, and product structures involved in these pathways are shown in Figure S3.

Table 3. Intermediates relative energy E_{ad} (kcal/mol), reaction energy barrier E_b (kcal/mol), and reaction heat E_r (kcal/mol) of the C–H and C–S bond dissociation reactions of C_2H_6OS on the OH pre-adsorbed CuO(111) surface.

Reaction Path	Bond That Is Broken	E_{ad}	E_b	E_r
$H \rightarrow O_{suf}$	C–H	–32.9	27.2	23.3
$H \rightarrow OH_{suf}$	C–H	–32.9	20.0	16.7
$H \rightarrow O_{sub}$	C–H	–32.9	40.5	30.1
$-CH_3 \rightarrow Cu_{suf}$	C–S	–32.9	57.8	34.4
$-CH_3 \rightarrow O_{suf}$	C–S	–32.9	60.4	1.9
$-CH_2 \rightarrow O_{suf}$	C–S	–16.2	19.3	–17.2
$H \rightarrow O_{sub}$	C–H	–16.2	28.0	12.7
$H \rightarrow O_{suf}$	C–H	–16.2	43.9	17.5

Figure 5 shows that transferring a H atom from C_2H_6OS to OH to form H_2O on the OH preadsorbed CuO(111) surface requires passing through a transition state, TS1', and generates an intermediate species, IM2'. Evidently from Table 3, the energy barrier for this process was only 20.0 kcal/mol, which is lower than the barriers for H transfers to the O_{suf} and O_{sub} sites to form C_2H_5OS , which were 27.2 and 40.5 kcal/mol, respectively. Moreover, transferring $-CH_3$ in C_2H_6OS to the Cu_{suf} or O_{suf} site incurs higher energy barriers (57.8 and 60.4 kcal/mol, respectively), as shown in Table 3. Therefore, when a C_2H_6OS molecule is adsorbed onto the OH preadsorbed CuO(111) surface, the initial reaction is the cleavage of the C–H bond, thereby resulting in the generation of C_2H_5OS and H. The cleaved H then combined with the surface OH to form H_2O , whereas the S atom in the intermediate species C_2H_5OS formed a stable chemical bond with the Cu_{sub} atom on the surface, with a bond length of 2.281 Å (IM2' in Figure 5). Furthermore, the energy barrier of 20.0 kcal/mol for the C–H bond cleavage is approximately 15 kcal/mol lower than that on the pure CuO(111) surface. Therefore, the presence of preadsorbed OH significantly enhanced the dehydrogenation of C_2H_6OS compared with that on pure CuO(111) surfaces.

Furthermore, the C–H and C–S bond cleavage of the intermediate IM2' on the OH preadsorbed CuO(111) surface was investigated. Three primary reaction pathways were identified: transfer of $-CH_2$ from C_2H_5OS to O_{suf} atoms, and transfer of H atom to O_{sub} or O_{suf} atoms. The calculations of Gibbs free energy changes revealed that transferring $-CH_2$ to the O_{suf} site was thermodynamically stable and spontaneous, with a Gibbs free energy change of -17.0 kcal/mol, which is more negative than on the pure CuO(111) surface, thus indicating that the C–S bond cleavage trend on the OH-preadsorbed CuO(111) surface was greater. By contrast, transferring H to the O_{sub} and O_{suf} sites resulted in positive Gibbs free energy changes of 10.3 and 16.7 kcal/mol, respectively, which must be overcome to achieve the reaction. The energy barrier for transferring $-CH_2$ to the O_{suf} site was 19.3 kcal/mol through transition state TS2', whereas transferring H had energy barriers of 28.0 and 43.9 kcal/mol to the O_{sub} and O_{suf} sites, respectively. These results suggest that the transfer of $-CH_2$ to the O_{suf} site is a favorable reaction pathway that is both thermodynamically and kinetically feasible. The energy barrier of this pathway is approximately 20 kcal/mol lower than that of a pure CuO(111) surface (38.1 kcal/mol). Thus, the presence of preadsorbed OH on the CuO(111) surface promotes the C–S bond cleavage of C_2H_6OS compared with the pure CuO(111) surface.

4. Conclusions

This study aimed to investigate the mechanism of CuO on oil shale and its surface modification from the atomic and molecular levels. Considering the complexity of the molecular structure and pyrolysis process of kerogen in oil shale, C_2H_6OS was used as a representative model molecule. Periodic models and first-principle calculations based on the

DFT were used. Two distinct reaction environments were analyzed to compare the catalytic effects of different CuO(111) surfaces: pure and OH preadsorbed CuO(111) surfaces.

The findings herein indicate that C₂H₆OS interacts primarily with the Lewis acid site of both surfaces through O and S atoms, thus leading to strong chemical adsorption. On both surfaces, C₂H₆OS tended to break the C-H bond first, followed by the C-S bond, which is different from the order of bond energies for C-H and C-S bonds [31,32]. Notably, besides the stronger adsorption affinity of Cu_{sub} atoms towards molecules, as reported in the literature [12], the O_{suf} atom demonstrated favorable reactivity, attracting both H and -CH₂ fragments formed by the decomposition of C₂H₆OS. On the pure CuO(111) surface, C₂H₆OS removed one H to O_{suf} first, followed by breakage of the C-S bond to remove one -CH₂ atom from O_{suf}. However, on the OH preadsorbed CuO(111) surface, C₂H₆OS initially removed one H to OH on the surface and then broke the C-S bond to remove one -CH₂ from O_{suf}. The activation energies for dehydrogenation and C-S bond cleavage were significantly lower, measuring 20.0 and 19.3 kcal/mol, which are 41% and 49% lower than those on the pure surface, respectively. These results suggest that the presence of OH greatly facilitates the surface decomposition of C₂H₆OS. They also indicate a potential risk of long-term storage of C₂H₆OS and CuO leading to hazardous conditions. These findings are helpful for understand the catalytic transformation mechanism of nano-CuO into oil shale and provide a theoretical basis for the design and synthesis of catalysts for the thermal transformation of oil shale. Additionally, they provide valuable data to evaluate the thermal hazards of C₂H₆OS when combined with incompatible substances. Future studies will explore alternative surface modification techniques, such as metal atom doping, to further enhance the catalytic activity of CuO in oil shale cracking.

Supplementary Materials: The following supporting information can be downloaded at: <https://www.mdpi.com/article/10.3390/pr11061781/s1>, Figure S1: The intermediates, transition states and product structures involved in the three main reaction paths of C₂H₆OS on the pure CuO(111) surface; Figure S2: Structures of C₂H₅OS (i.e., IM2 in Figure 5) breaking C-S bond on the perfect CuO(111) surface; Figure S3: Structures of the intermediates, transition states and product involved in various reaction pathways for DS-OH-4 to break C-H or C-S bond.

Author Contributions: Conceptualization, Y.-Q.W., X.-L.M. and J.-Z.S.; Data curation, H.-H.X.; Methodology, Y.-Q.W. and X.-L.M.; Project administration, W.-C.Y.; Resources, J.-Z.S.; Software, L.-L.L.; Supervision, W.-C.Y.; Writing—original draft, Y.-Q.W. All authors have read and agreed to the published version of the manuscript.

Funding: This research was funded by the National Oil Shale Research and Development Center Foundation of China (33550000-21-ZC0611-0013), National Key Research And Development Project (2019YFA0705503), and Sinopec Science and Technology Project (P20066).

Institutional Review Board Statement: Not applicable.

Informed Consent Statement: Not applicable.

Data Availability Statement: The datasets used and/or analyzed during the current study are available from the corresponding author on reasonable request.

Conflicts of Interest: The authors declare no conflict of interest.

References

1. Hu, M.; Cheng, Z.; Zhang, M.; Liu, M.; Song, L.; Zhang, Y.; Li, J. Effect of calcite, kaolinite, gypsum, and montmorillonite on Huadian oil shale kerogen pyrolysis. *Energy Fuels* **2014**, *28*, 1860–1867. [CrossRef]
2. Yu, H.; Li, S.; Jin, G. Catalytic hydrotreating of the diesel distillate from Fushun shale oil for the production of clean fuel. *Energy Fuels* **2010**, *24*, 4419–4424. [CrossRef]
3. Mahboob, I.; Shafiq, I.; Shafique, S.; Akhter, P.; Amjad, U.; Hussain, M.; Park, Y. Effect of active species scavengers in photocatalytic desulfurization of hydrocracker diesel using mesoporous Ag₃VO₄. *Chem. Eng. J.* **2022**, *441*, 136063. [CrossRef]
4. Chen, M.; Li, C.; Li, G.R.; Chen, Y.L.; Zhou, C.G. In situ preparation of well-dispersed CuO nanocatalysts in heavy oil for catalytic aquathermolysis. *Pet. Sci.* **2019**, *16*, 439–446. [CrossRef]

5. Zhong, Y.T.; Tang, X.D.; Li, J.J.; Zhou, T.D.; Deng, C.L. Thermocatalytic upgrading and viscosity reduction of heavy oil using copper oxide nanoparticles. *Pet. Sci. Technol.* **2020**, *38*, 891–903. [[CrossRef](#)]
6. Tverdov, I.; Khafizov, N.R.; Madzhidov, T.I.; Varfolomeev, M.A.; Yuan, C.; Kadkin, O.N. Theoretical Insights into the Catalytic Effect of Transition-Metal Ions on the Aquathermal Degradation of Sulfur-Containing Heavy Oil: A DFT Study of Cyclohexyl Phenyl Sulfide Cleavage. *ACS Omega* **2020**, *5*, 19589–19597. [[CrossRef](#)]
7. Xia, H.; Meng, X.; Jiang, X.; Lu, L.; Wang, Y. Theoretical Investigation on the Catalytic Effect and Mechanism of Pure and Cu–Doped SBA–15 Molecular Sieves on the Decomposition of Dimethyl Sulfoxide. *Processes* **2023**, *11*, 1386. [[CrossRef](#)]
8. Wang, S.; Song, L.; Jiang, X. Catalytic effects of Fe- and Ca-based additives on gas evolution during pyrolysis of Dachengzi oil shale of China. *Oil Shale* **2018**, *35*, 39–55. [[CrossRef](#)]
9. Lu, Y.; Wang, Y.; Wang, Q.; Zhang, J.; Zhao, Y.; Zhang, Y. Investigation on the catalytic effect of AAEMs on the pyrolysis characteristics of Changji oil shale and its kinetics. *Fuel* **2020**, *267*, 117287. [[CrossRef](#)]
10. Li, J.; Sun, X.; Wu, D.; Zhai, S.; Yang, S.; Toktonaliev, A.; Pan, Y. Application of Oil Shale Molecular Sieve Catalyst: A Review. *Chem. Technol. Fuels Oils* **2022**, *58*, 902–911. [[CrossRef](#)]
11. Guo, Y.; Hu, R.; Zhou, X.; Yu, J.; Wang, L. A first principle study on the adsorption of H₂O₂ on CuO (111) and Ag/CuO (111) surface. *Appl. Surf. Sci.* **2019**, *479*, 989–996. [[CrossRef](#)]
12. Ahmad, F.; Agusta, M.K.; Maezono, R.; Dipojono, H.K. DFT+U study of H₂O adsorption and dissociation on stoichiometric and nonstoichiometric CuO (111) surfaces. *J. Phys. Condens. Matter* **2019**, *32*, 045001. [[CrossRef](#)]
13. Ye, X.; Jiao, A.; Zhang, H.; Chen, B.; Wang, S.; Shen, J.; Yan, Z.; Deng, S.; Han, X.; Jiang, X.; et al. Quantum chemical calculations for the H free radical chemisorption with different chain models during oil shale pyrolysis. *Fuel* **2021**, *290*, 119999. [[CrossRef](#)]
14. Tian, Z.; Chen, B.; Qiu, X.; Liu, W.; Guo, Y. Study of quantum chemistry calculation simulation for the effect of electric field on the kerogen molecular decomposition. *Fuel* **2022**, *318*, 123584. [[CrossRef](#)]
15. Chen, B.; Zhou, C.; Qin, L.; Fan, K.; Xue, J.; Guo, Y. Quantum chemistry simulation and kinetic analysis of organic nitrogen transfer during oil shale pyrolysis. *Energy* **2022**, *256*, 124709. [[CrossRef](#)]
16. Kang, S.; Sun, Y.; Qiao, M.; Li, S.; Deng, S.; Guo, W.; Li, J.; He, W. The enhancement on oil shale extraction of FeCl₃ catalyst in subcritical water. *Energy* **2022**, *238*, 121763. [[CrossRef](#)]
17. Delley, B. From molecules to solids with the DMol3 approach. *J. Chem. Phys.* **2000**, *113*, 7756–7764. [[CrossRef](#)]
18. Perdew, J.P.; Burke, K.; Ernzerhof, M. Generalized gradient approximation made simple. *Phys. Rev. Lett.* **1996**, *77*, 3865. [[CrossRef](#)]
19. White, J.A.; Bird, D.M. Implementation of gradient-corrected exchange-correlation potentials in Car-Parrinello total-energy calculations. *Phys. Rev. B* **1994**, *50*, 4954. [[CrossRef](#)]
20. Becke, A.D. A multicenter numerical integration scheme for polyatomic molecules. *J. Chem. Phys.* **1988**, *88*, 2547–2553. [[CrossRef](#)]
21. Inada, Y.; Orita, H. Efficiency of numerical basis sets for predicting the binding energies of hydrogen bonded complexes: Evidence of small basis set superposition error compared to Gaussian basis sets. *J. Comput. Chem.* **2008**, *29*, 225–232. [[CrossRef](#)] [[PubMed](#)]
22. Hu, R.; Zhou, X.; Yu, J. The effect of surface structure on Ag atom adsorption over CuO (111) surfaces: A first principles study. *Appl. Surf. Sci.* **2017**, *425*, 1111–1117. [[CrossRef](#)]
23. Maimaiti, Y.; Nolan, M.; Elliott, S.D. Reduction mechanisms of the CuO (111) surface through surface oxygen vacancy formation and hydrogen adsorption. *Phys. Chem. Chem. Phys.* **2014**, *16*, 3036–3046. [[CrossRef](#)] [[PubMed](#)]
24. Suo, W.; Sun, S.; Liu, N.; Li, X.; Wang, Y. The adsorption and dissociation of N₂O on CuO (111) surface: The effect of surface structures. *Surf. Sci.* **2020**, *696*, 121596. [[CrossRef](#)]
25. Hohenberg, P.; Kohn, W. Inhomogeneous electron gas. *Phys. Rev.* **1964**, *136*, B864. [[CrossRef](#)]
26. Grimme, S.; Antony, J.; Ehrlich, S.; Krieg, H. A consistent and accurate ab initio parametrization of density functional dispersion correction (DFT-D) for the 94 elements H–Pu. *J. Chem. Phys.* **2010**, *132*, 154104. [[CrossRef](#)]
27. Fischer, T.H.; Almlof, J. General methods for geometry and wave function optimization. *J. Phys. Chem.* **1992**, *96*, 9768–9774. [[CrossRef](#)]
28. Govind, N.; Petersen, M.; Fitzgerald, G.; King-Smith, D.; Andzelm, J. A generalized synchronous transit method for transition state location. *Comput. Mater. Sci.* **2003**, *28*, 250–258. [[CrossRef](#)]
29. Hu, J.; Li, D.; Lu, J.G.; Wu, R. Effects on electronic properties of molecule adsorption on CuO surfaces and nanowires. *J. Phys. Chem.* **2010**, *114*, 17120–17126. [[CrossRef](#)]
30. Wang, Y.Q.; Lu, L.L.; Lai, L.; Wang, B.S. Comparison of interactions between aluminium hydride oxide surfaces and three energetic plasticizers: DFT calculations. *Appl. Surf. Sci.* **2019**, *488*, 237–245. [[CrossRef](#)]
31. Shokrlu, Y.H.; Babadagli, T. Viscosity reduction of heavy oil/bitumen using micro- and nano-metal particles during aqueous and non-aqueous thermal applications. *J. Pet. Sci. Eng.* **2014**, *119*, 210–220. [[CrossRef](#)]
32. Shokrlu, Y.H.; Babadagli, T. In-situ upgrading of heavy oil/bitumen during steam injection by use of metal nanoparticles: A study on in-situ catalysis and catalyst transportation. *SPE Reserv. Eval. Eng.* **2013**, *16*, 333–344. [[CrossRef](#)]

Disclaimer/Publisher’s Note: The statements, opinions and data contained in all publications are solely those of the individual author(s) and contributor(s) and not of MDPI and/or the editor(s). MDPI and/or the editor(s) disclaim responsibility for any injury to people or property resulting from any ideas, methods, instructions or products referred to in the content.